

1 **An optimal XBT-based monitoring system for the South Atlantic**
2 **Meridional Overturning Circulation at 34°S**

3 MARLOS GOES^{1,2} * , GUSTAVO J. GONI², AND SHENFU DONG^{1,2}

¹ *CIMAS, University of Miami, Miami, FL, United States*

² *PHOD, NOAA/AOML, Miami, FL, United States.*

Submitted to JTECH

November, 26, 2013

* *Corresponding author:* Marlos Goes, Cooperative Institute for Marine and Atmospheric Studies, Rosenstiel School of Marine and Atmospheric Science, University of Miami, 4600 Rickenbacker Causeway, Miami, FL, 33149,

E-mail: mgoes@rsmas.miami.edu and marlos.goes@noaa.gov .

ABSTRACT

4
5 The South Atlantic is an important pathway for the inter-basin exchanges of heat and fresh-
6 water with strong influence on the global meridional overturning stability and variability.
7 Along the 34°S meridian, a quarterly, high resolution XBT transect (AX18) samples the
8 temperature structure in the upper ocean, and has been shown to be a useful component
9 of a meridional overturning monitoring system of the region. However, an optimal design
10 for an XBT-based system has not yet been developed. Here we use a high-resolution ocean
11 assimilation product to simulate an XBT-based observational system across the South At-
12 lantic. The sensitivity of the meridional heat transport, meridional overturning circulation,
13 and geostrophic velocities to key observational assumptions is studied. Key assumptions
14 taken into account are horizontal and temporal sampling of the transect, salinity and deep
15 temperature inference, as well as the level of reference for geostrophic velocities. With the
16 current sampling strategy, the largest errors in the meridional overturning and heat transport
17 estimations are the reference velocity for geostrophic calculations and the western bound-
18 ary resolution. We use the results obtained by the state estimation under observational
19 assumptions to make recommendations for potential improvements in the AX18 transect
20 implementation.

21 1. Introduction

22 The Atlantic Ocean circulation is ubiquitous for having a deep convection site at high
23 latitudes in the northern hemisphere, which drives to a large extent the Atlantic merid-
24 ional overturning circulation (AMOC) and, therefore, the northward heat transport to the
25 northern latitudes. The variability of the AMOC circulation is responsible for changes in the
26 northern hemisphere climate and may impact the climate globally (e.g., Zhang and Delworth
27 2005). Despite the high control of the AMOC strength and variability in the North Atlantic
28 Subpolar gyre, the deep convection regions between the Greenland-Iceland-Scotland seas
29 are highly sensitive to heat and freshwater transported from the South Atlantic (Rahmstorf
30 1996; Donners and Drijfhout 2004), which is suggested to be one of the main drivers of two
31 stable states of the AMOC (Weijer et al. 1999; Beal et al. 2011; Hawkings et al. 2011; Garzoli
32 et al. 2013).

33 The South Atlantic is a source and sink of heat and mass, with important contributions
34 from fluxes from other basins through, for example, the Agulhas current region (Goni et al.
35 1997) and the Brazil-Malvinas confluence region (Gordon 1986; Wainer et al. 2000; Goni
36 and Wainer 2001; Goni et al. 2011). The South Atlantic Ocean has been historically one
37 of the least observed regions on the globe; however, several efforts to measure long-term
38 variability in the basin have been put forward in the last decade. For instance, expendable
39 bathythermograph (XBT) observations from the high-density XBT transect AX18 (Figure
40 1a) measures temperature in the upper 800 m of the ocean four times a year along 34°S. Stud-
41 ies based on the AX18 XBT data have shown that the mean AMOC and heat transport at
42 34°S are mostly geostrophically driven, although the wind-driven Ekman component equally
43 contributes to the variability of the meridional transports (Dong et al. 2009). Compensation
44 between the Ekman and geostrophic components may translate into a small annual cycle of
45 heat and volume transports (Garzoli and Baringer 2007; Dong et al. 2009), although models
46 generally do not reproduce this characteristic (Dong et al. 2011b).

47 Currently, observational estimates rely on several assumptions to estimate the integral

48 flow in the South Atlantic. Thus far, only Baringer and Garzoli (2007) have estimated the
49 uncertainty resulting from the underlying XBT-based observational system methodological
50 assumptions to measure heat transport across 34°S. However, no sensitivity tests have yet
51 been performed to optimize the AX18 sampling strategy in order to maximize the informa-
52 tion content, and to assess the uncertainty in volume and heat transports associated with
53 observational and computational methodologies across 34°S. To accomplish this, current
54 high resolution ocean reanalyses can be useful to assess and investigate potential improve-
55 ments in the sampling strategy of the AX18 transect using observing system simulations
56 methodologies. Similar methodologies have been applied, for example, in several studies in
57 the North Atlantic (e.g. Hirschi et al. 2003; Baehr et al. 2004, 2008) to evaluate strategies
58 for monitoring the MOC in the North Atlantic.

59 The aim of the present study is to assess how observational and computational method-
60 ologies affect the estimates of volume and heat transports across 34°S in Atlantic Ocean,
61 and how to optimize the design of the AX18 XBT transect in order to reduce uncertainty
62 estimates. Therefore, this study will address four main objectives to evaluate the AX18 XBT
63 transect:

- 64 i) The optimal spatial (longitudinal) resolution.
- 65 ii) The optimal temporal sampling to capture the seasonal variability of the AMOC in
66 the region.
- 67 iii) The uncertainties derived from the salinity and deep temperature estimation.
- 68 iv) Potential improvements to the assumptions made regarding the level of reference to
69 resolve the barotropic mode.

70 To address these goals, we will first describe the characteristics of the region of study
71 (Section 2). We will use a high-resolution global assimilation model (Section 3) that compares
72 reasonably well with the regional observations and characteristics presented in Section 2. We
73 will define the methodology (Section 4) to calculate volume and meridional heat transport
74 across 34°S, and perform controlled experiments in the model framework to answer point-

75 by-point the above questions (Section 5). Finally, we will discuss the results and make
76 recommendations for the improvement of the AX18 XBT transect measurements (Section
77 6).

78 **2. Regional characteristics**

79 The subtropical South Atlantic is characterized by a large scale anticyclonic feature, the
80 South Atlantic subtropical gyre (Stramma and England 1999; Garzoli and Matano 2011). In
81 the southwestern Atlantic, the surface dynamics are dominated by the Brazil-Malvinas Con-
82 fluence, which is characterized by the cold northward flow of the Malvinas Current, and a
83 southward flowing warm weak western boundary current, the Brazil Current (Garzoli 1993).
84 This region exhibits complex frontal motions (Goni et al. 2011; Goni and Wainer 2001) and
85 patterns with the simultaneous presence of warm and cold rings and eddies (Lentini et al.
86 2006) and, therefore, it is characterized by large values of eddy kinetic energy (Figure 1a).
87 In the southeastern Atlantic, the transfer of warm waters from the Indian Ocean into the
88 South Atlantic subtropical gyre largely takes place in the form of rings and filaments formed
89 when the Agulhas Current retroflects south of Africa between 1°W and 25°E (Richardson
90 and Garzoli 2003; Goni et al. 1997). The eastward flowing South Atlantic Current and the
91 northward flowing Benguela Current complete the circulation, delimiting the southern and
92 eastern boundaries of the subtropical gyre, respectively. The Brazil-Malvinas Confluence re-
93 gion and the Agulhas retroflexion region represent the most energetic areas contained in the
94 region of study. These two regions present similar values of mean eddy kinetic energy, above
95 $1000 \text{ cm}^2 \text{ s}^{-2}$ (Figure 1a), as observed by altimetric sea level anomalies (Ducet et al. 2000)
96 for the 2007-2012 time period. The Brazil-Malvinas Confluence and Agulhas retroflexion
97 regions are both crossed by the XBT transect AX18 (Figure 1a).

98 **3. The HYCOM-NCODA reanalysis**

99 As suggested in previous studies, the strong mesoscale energy in the South Atlantic region
100 requires a minimum of eddy-permitting models to resolve its main features (Treguier et al.
101 2007; Biastoch et al. 2009). In the present study we use data from the Hybrid Coordinate
102 Ocean Model (HYCOM)-Navy Coupled Ocean Data Assimilation (NCODA) assimilative
103 product (Chassignet et al. 2009), encompassing a total of nearly 6 years of model simulation,
104 sampled in a 7-day timestep using 7-day averages. We combine three experiments, numbered
105 as GLBa0.08/74.2 (June 2007 to September 2008), GLBa0.08/expt_90.6 (September 2008 to
106 May 2009), and GLBa0.08/expt_90.8 (May 2009 to May 2013) in order to maximize the
107 temporal coverage of the model output.

108 The HYCOM-NCODA is configured for the global ocean with HYCOM 2.2 as the dy-
109 namical model. Computations are carried out on a Mercator grid between 78°S and 47°N,
110 with an average of 1/12° (~ 7 km) horizontal spacing and 32 vertical layers. A bipolar patch
111 is used for regions north of 47°N. Bathymetry is derived from the U. S. Naval Research
112 Laboratory 2-minute DBDB2 (Digital Bathymetric Data Base) dataset. Surface forcing is
113 from the Navy Operational Global Atmospheric Prediction System (NOGAPS) and includes
114 3-hourly and 0.5° wind stress, wind speed, heat flux (using bulk formula), and precipitation.
115 The NCODA methodology (Cummings 2005) uses the model forecast as a first guess in a
116 multi-variate Optimal Interpolation (MVOI) scheme and assimilates available along-track
117 satellite sea height anomaly observations (obtained via the NAVOCEANO Altimeter Data
118 Fusion Center), in-situ sea surface temperature (SST), as well as available in-situ vertical
119 temperature and salinity profiles from XBTs, ARGO floats and moored buoys. MODAS
120 synthetic profiles are used by NCODA for downward projection of surface information (Fox
121 et al. 2002).

122 Compared to altimetric observations, the eddy-resolving HYCOM-NCODA reanalysis
123 reproduces reasonably the main circulation features of the region (Figure 1b). The output
124 of this model, however, shows lower energy in the Brazil-Malvinas Confluence and Agulhas

125 retroflection regions (Figure 1c). Low biases are generally on the order of $-300 \text{ cm}^2 \text{ s}^{-2}$ or
 126 lower, which is also observed in the comparison of the sea level root-mean square variability
 127 of the region (Figure 2a, b). We select 18 realizations (Figure 2a) of the AX18 transect
 128 based on the criteria of being zonally directed (median angle $< 10^\circ$, and with the mean
 129 section between 30° and 36° of latitude) to compare the model thermohaline behavior with
 130 the actual XBT observations along the nominal 34°S . Below 850 m, the maximum depth
 131 sampled by the XBTs, the WOA05 annual climatology (Locarnini et al. 2006) is used. The
 132 mean temperature section retrieved by the AX18 along the nominal of 34°S shows an east-
 133 west gradient, with higher temperatures in the west (Figure 2b, c). The associated zonal
 134 density gradients allow average geostrophic volume and heat transports to the north, as
 135 shown in previous studies (e.g., Ganachaud and Wunsch 2003; Garzoli and Baringer 2007).
 136 The model shows generally negative temperature biases in the interior (~ 1 to 2°C) and
 137 positive biases on the boundaries (~ 1 to 1.5°C) relative to the mean AX18 section above
 138 850 m, and stronger stratification on the bottom of the ocean in comparison to the WOA05
 139 climatology (Figure 2g-i).

140 4. Methodology

141 This study focuses on the reconstruction of the AMOC streamfunction (PSI_y) and the
 142 heat transport (MHT) along 34°S by simulating XBT observations. This section describes
 143 how the AMOC and MHT are defined through the paper.

144 a. AMOC

145 The AMOC streamfunction is defined as:

$$PSI_y(z) = \int_{x_E}^{x_W} \int_z^{-H} v(x, z) dx dz \quad (1)$$

146 i.e., the integral of the meridional velocity $v(x,z)$ from the bottom (H) to the depth (z)
 147 of the ocean and between the western (x_W) and the eastern (x_E) boundaries of the basin.
 148 The meridional velocity $v(x,z)$, and therefore its derived meridional streamfunction, can be
 149 decomposed into three dynamical components (Lee and Marotzke 1998):

$$v(x, z) = \frac{1}{H} \int_{-H}^0 v(x, z) dz + [v_E(x, z) - \frac{1}{H} \int_{-H}^0 v_E(x, z) dz] + v_{sh}(x, z) \quad (2)$$

150 where the first term on the right hand side of Equation (2) is known as the barotropic or gyre
 151 component (v_{bar}), which is here defined as the local average of $v(x,z)$ over the depth H of
 152 the ocean, the second term is the Ekman component compensated by a depth-independent
 153 flow, and the last term is the vertical shear component, which consists of the velocities
 154 calculated using the thermal wind relationship. Other ageostrophic contributions (frictional
 155 and non-linear) are not defined. v_E is derived from the local zonal wind stress (τ_x):

$$v_E = -\frac{\tau_x}{\rho_0 f D_E} \quad (3)$$

156 where $\rho_0 = 1025 \text{ kg m}^{-3}$ is the mean water density, f the Coriolis parameter, and D_E is
 157 the depth of the Ekman layer, which is arbitrarily assumed here to be $D_E = 50 \text{ m}$ (e.g.,
 158 Pond and Pickard 1983). The barotropic and vertical shear velocities combined constitute
 159 the absolute geostrophic velocity, which is estimated using the dynamic method assuming a
 160 reference level (Pond and Pickard 1983). Barotropic velocities have a strong contribution to
 161 the geostrophic flow at locations of sloping topography, and their projection on the AMOC
 162 can therefore be an important term in the AMOC reconstruction (Baehr et al. 2004).

163 The AMOC strength (in Sv) is further defined as the value of the maximum amplitude of
 164 the AMOC streamfunction. The same definition is applied for the strength of the individual
 165 components of the AMOC.

166 *b. Meridional Heat Transport*

167 The meridional heat transport is calculated as follows:

$$MHT = \rho_0 c_p \int_{-H}^0 \int_{x_E}^{x_W} v(x, z) \theta(x, z) dx dz - \rho_0 c_p M_y \langle \theta \rangle \quad (4)$$

168 where $c_p = 4187 \text{ J kg}^{-1} \text{ K}^{-1}$ is the specific heat of sea water, and $\langle \theta \rangle$ is the averaged potential
 169 temperature θ along the section. The second term in Equation (4) is a constraint to allow
 170 zero mass transport across the section, which is necessary for heat transport calculations in
 171 free surface models, since they do not necessarily have zero mass transport at any given time
 172 period Jayne and Marotzke (2001); Griffies et al. (2004).

173 To reconstruct MHT, Equation (4) is further decomposed into the same components as
 174 the meridional overturning, using the corresponding decomposition of the velocity (Equation
 175 2). Following (Hall and Bryden 1982):

$$MHT = \rho_0 c_p \int_{-H}^0 \int_{x_E}^{x_W} v_{bar} \theta_{bar} dx dz + \int_{-H}^0 \int_{x_E}^{x_W} v_{vs} [\theta - \theta_{bar}] dx dz + \int_{-H}^0 \int_{x_E}^{x_W} v_{Ek} \theta_{Ek} dx dz \quad (5)$$

176 where θ_{bar} is the depth-averaged potential temperature, and θ_{ek} follows the Ekman velocity
 177 definition, i.e., θ_{ek} assumes only two values over depth, one as the average in the Ekman
 178 layer, and another in the layer below the Ekman layer. Each of the terms in Equation
 179 (5) is meaningful as a heat transport, because the velocity components are design to be
 180 compensated and allow zero net volume transport across the section (Hirschi et al. 2003).
 181 Otherwise, the calculated heat transport would be dependent on an arbitrary temperature
 182 reference (Montgomery 1974).

183 5. Results

184 *a. AMOC streamfunction reconstruction*

185 The AMOC strength calculated from the model output velocities in a 7-day average is
 186 highly variable in time (Figure 3a; black line), with amplitude ranging from -8 to 35 Sv (1 Sv

187 $= 10^6 \text{ m}^3\text{s}^{-1}$), and with strong high frequency variability as well as a defined annual cycle.
188 The time-averaged AMOC streamfunction (Figure 3b) shows positive (northward) values in
189 the upper 3500 m, negative (southward) values underneath, and a pronounced maximum at
190 the depth of ~ 1500 m, which characterizes the AMOC strength. The AMOC strength in
191 the model is 15.1 ± 7.6 Sv, lower than observational estimates of 17.9 ± 2.2 Sv (Dong et al.
192 2009), but within the uncertainty estimates. High resolution models, such as the OFES
193 model (Dong et al. 2011b), show a strong agreement with the AMOC strength value (15.0
194 ± 3.7 Sv) presented here.

195 We decompose the AMOC streamfunction into its vertical shear, Ekman, and barotropic
196 components using the methodology described in Section 4a. Therefore, each component is
197 independently estimated, accordingly to Lee and Marotzke (1998) and Baehr et al. (2004),
198 but differently from the methodologies of Perez et al. (2011) and Dong et al. (2011b), which
199 estimate the geostrophic transport either unbalanced for mass transport or as the residual
200 between the total and Ekman transports. The absolute geostrophic component (barotropic
201 plus vertical shear) is calculated by using a level of known motion at the bottom of the ocean,
202 assuming that velocities are perfectly known there. The vertical shear component has the
203 strongest contribution to the total AMOC strength (Figure 3b), with an average of 26.9 ± 3.1
204 Sv, and it is in great part compensated by the barotropic contribution of the transport, which
205 is negative (southward) with an average of -15.9 ± 6 Sv. The resulting absolute geostrophic
206 transport is 11 ± 6.7 Sv, smaller than the observational value of 15.7 ± 2.6 Sv (Dong et al.
207 2009) and that obtained from the OFES model (12.9 ± 2.1 Sv; Dong et al. (2011b)). It is
208 worth mentioning that neither the barotropic nor the vertical shear streamfunctions show
209 a reversal in depth, as observed on the total mean streamfunction, but that the addition
210 of these two streamfunctions produces the same reversal pattern at approximately 3500
211 m (magenta line in Figure 3c) as observed in the original model streamfunction. Strong
212 interannual variability is observed in the barotropic component, with positive anomalies in
213 the austral summer of 2007 and 2008 and negative anomalies in the austral spring of 2009

214 and 2010. The Ekman component has the lowest contribution to the mean AMOC strength,
215 only 2 ± 4 Sv, but its maximum amplitude can reach over 10 Sv, which is similar to the
216 other components.

217 The MHT follows the same pattern as the AMOC (Figure 4). The mean MHT calculated
218 directly from the model fields is 0.33 ± 0.5 PW (1 PetaWatt = 10^{15} W), which is also lower
219 than the values calculated from observational studies (0.54 ± 0.14 PW; Garzoli et al. (2013)).
220 The barotropic MHT component (-0.6 ± 0.23 PW) compensates to a large extent the vertical
221 shear component (0.8 ± 0.35 PW), and the Ekman component contributes about one third
222 of the total MHT (0.12 ± 0.24 PW).

223 The annual variability of the AMOC and MHT components (Figure 5) shows that
224 the vertical shear component does not have a noticeable annual cycle. The Ekman and
225 barotropic components have stronger annual cycles, and are approximately in phase with
226 each other, with more positive/less negative values from March to August. Therefore, the
227 total geostrophic transport (vertical shear plus barotropic) and the Ekman components have
228 similar phases, a result that is at odds with previous observational studies (e.g., Dong et al.
229 2009) that show an out-of-phase relationship between the Ekman and geostrophic AMOC
230 annual cycle, which produces a much reduced annual cycle of the AMOC variability. How-
231 ever, other high-resolution models also show a similar annual cycle for the total AMOC (e.g.,
232 Dong et al. 2011b; Perez et al. 2011) as observed here. The residual contribution, which is
233 the part of the annual variance that is not explained by the reconstruction (cyan line, Figure
234 5), is negligible for the AMOC but can reach up to 0.5 PW for the MHT, especially dur-
235 ing the austral summer. As observed in Figure 4a, the model MHT is weak or sometimes
236 negative during austral summer, but these reversals of MHT are not featured in the recon-
237 struction (Figure 4a, magenta line). These differences may be associated with ageostrophic
238 terms other than Ekman (Sime et al. 2006), non-linearities in the MHT calculation, and
239 unbalanced flow of volume (0.94 ± 3.8 Sv), whose MHT contribution is here estimated at
240 -0.02 ± 0.06 PW, the same mean value of 0.02 PW estimated in Baringer and Garzoli (2007).

241 Other methodologies also show a stronger reconstructed MHT in comparison with the di-
242 rect estimates from models (Perez et al. 2011). Surprisingly, the mean of the reconstructed
243 MHT, which is higher than the original timeseries, is 0.54 PW, the same value as estimated
244 by Garzoli and Baringer (2007) and Garzoli et al. (2013) using XBT observations.

245 *b. XBT observational strategy*

246 The AX18 XBT transect, which was designed with the main purpose of monitoring the
247 variability of the upper limb of the AMOC transport, measures temperature in the upper
248 ocean between Cape Town and South America quarterly, with a high-density (between 25-50
249 km) zonal spacing.

250 Observational studies that used AX18 data to estimate meridional volume and heat
251 transports involved several methodological assumptions. The XBTs measure temperature
252 profiles in the upper 800 m depth (e.g. Deep Blue probe type). Because XBTs do not
253 measure salinity, a common method to infer salinity profiles at an XBT deployment location
254 uses a lookup table derived from historical temperature-salinity (T-S) relationships (Thacker
255 2008). Below 800 m, the temperature and salinity profiles are extended down to the bottom
256 of the ocean with their climatological values (Baringer and Garzoli 2007; Dong et al. 2009).
257 The barotropic or external mode is generally estimated by adopting a level of no motion at
258 the depth where the potential density anomaly referenced to 2000 dbar assumes the value
259 of 37.09 Kg m^{-3} ($\sigma_2 = 37.09$). The $\sigma_2 = 37.09$ depth is approximately located at 3700
260 m depth and between two water masses, the North Atlantic Deep Water (NADW) flowing
261 southward between 1500 and 3700 m, and the underlying Antarctic Bottom Water (AABW)
262 flowing northward (Ganachaud and Wunsch 2003; Baringer and Garzoli 2007). The Ekman
263 component of the flow is calculated from available zonal wind stress products at the XBT
264 deployment locations.

265 In order to simulate the XBT observations in the model, we make the same assumptions
266 as used in the observational studies: i) the model temperature data are used above 800 m,

267 ii) a quadratic least squares fit between the annual mean temperature and salinity obtained
268 from the model is specified for each depth, calculated using 1 degree boxes along 34°S, iii)
269 the monthly climatology of temperature and salinity at a 1 degree longitudinal resolution
270 is padded below 800 m to extend the pseudo-observations to the bottom of the ocean, and
271 iv) a reference level for the geostrophic velocity calculation is chosen. Constructing the T-S
272 relationships from the model instead of using, for example, the World Ocean Atlas (WOA)
273 climatology is necessary, since the model’s own internal biases relative to the observations
274 could potentially bring spurious T-S discontinuities. WOA climatology is subject to biases
275 in regional coverage, such as below 2000 m (the parking depth of Argo floats), along coastal
276 areas, and historically in the South Atlantic. Here, we do not account for imperfect sampling
277 although its effects can be sizeable in producing additional seasonal biases.

278 The RMS error between the model salinity and the salinity estimated from the lookup
279 table is shown in Figure 6. In the top 200 m, salinity errors are on the order of 0.1 psu.
280 Higher differences (~ 0.4 psu) are found in the western side of the basin in the upper 100
281 m, where there is a fresh water inflow from river runoff. Below 200 m the RMS difference
282 is generally lower than 0.1 psu, with higher values located around 500 m and decreasing to
283 near zero below 1000 m. These error values are on the same order of magnitude of the RMS
284 of the salinity annual cycle and, therefore, are highly driven by the seasonal variation of T-S
285 relationships, which is not captured by the annual mean T-S relationships.

286 It is also important to mention that XBT measurements do not contain pressure infor-
287 mation, and depth estimates follow a fall rate equation (FRE) that is a quadratic function
288 of the time of descent of the probe. The FRE is subject to parametric uncertainties, which
289 translate into depth biases with typical values of the order 2% of depth (Goes et al. 2013b).
290 The AMOC and MHT estimated errors associated with a typical FRE bias in the upper 800
291 m are -0.06 ± 0.07 Sv and -0.01 ± 0.01 PW, respectively, which are small compared to the
292 other observational assumptions considered here.

294 In this section we investigate the uncertainties associated with each of the assumptions
 295 applied in the AX18 transport estimates. We focus on the four main assumptions of the AX18
 296 transect design, which are i) temporal resolution, ii) horizontal resolution, iii) salinity and
 297 bottom temperature inferences, and iv) reference level for geostrophic velocity calculations.
 298 We apply each of the assumptions individually in order to quantify their uncertainties, which
 299 will allow recommending improvements in the AX18 transect design and implementation.

300 1) TEMPORAL RESOLUTION

301 The AX18 transect was originally implemented to be carried out four times a year, and
 302 estimates of the geostrophic AMOC transport can only be performed at the time of each
 303 AX18 transect realization. The rate of time sampling as well as the year-to-year variability
 304 of number of transects may alias the estimates of the annual cycle of the AMOC and merid-
 305 ional heat transport (Bryden et al. 2005). We simulate uncertainties associated with the
 306 transect temporal sampling in the model by randomly selecting snapshots of temperature
 307 and salinity sections, and differences in the geostrophic AMOC and MHT are used as metrics
 308 for the uncertainty estimation. We reproduce this simulation 400 times, which is a number
 309 sufficiently high to allow the average of all realizations to have the same monthly means
 310 as the original model geostrophic AMOC and MHT. Furthermore, the mean monthly RMS
 311 difference of the 400 realizations will define a measure of the uncertainty associated with the
 312 time sampling. We vary the simulated number of the AX18 realizations per year from 1 to
 313 20, and the number of years of data collection from 1 to 15. In order to extend the simulation
 314 beyond six years, the total period of the model simulation, we add to the original time series
 315 stretches of the original timeseries that were randomly selected, choosing the beginning of
 316 each stretch to match the timeseries seasonality. Contour plots showing the sampling error
 317 variability of the AMOC and MHT with respect to the number of years measured and the

318 number of samples per year is shown in Figure 7. The time sampling error of the AMOC and
319 MHT show similar behavior, i.e., errors decrease exponentially as more samples are collected
320 during the year or when a higher number of years is sampled. The RMS errors are as low as
321 0.5 Sv and 0.05 PW when carrying out up to 12 transect realizations per year for 15 years.
322 On the other hand, when transects are carried out twice a year for two years, the errors are
323 above 2.4 Sv and 0.25 PW, respectively. The current number of realizations of the AX18
324 transect along the nominal of 34°S is 18 (Figure 2), which are done approximately on a
325 quarterly basis. This is equivalent to a total sampling period of five years in our considered
326 parameter space. Therefore, according to our model estimates, the associated RMS errors
327 of the AMOC and MHT are 2.3 Sv and 0.24 PW, respectively (stars in Figure 7), close to
328 the most uncertain values in the studies parameter space. Although 12 realizations per year
329 is difficult to achieve operationally, current discussions for increasing the number of transect
330 realizations to five or six per year are underway. This would lower the RMS errors to < 2 Sv
331 for the AMOC and < 0.2 PW for the MHT, which may allow a greater improvement over
332 the years.

333 One additional temporal sampling error arises from the non-synopticity of the XBT
334 transect measurements. An AX18 realization takes approximately 10 days to complete the
335 trajectory from South America to Cape Town, which may alias the transport estimates
336 across this transect. We quantify here the errors due to non-synopticity by simulating the
337 same observational assumptions within the model environment. In this experiment, we
338 simulate one AX18 XBT realization by using 10 bins of meridional velocity values from east
339 to west that correspond to 10 consecutive days of model velocity. The AMOC and MHT
340 are estimated every 7 days from these simulations. These estimates are compared against
341 the ones from the synoptic model outputs, which are computed using the first day of each
342 daily simulation. The errors associated with the non-synopticity of the data for the whole
343 period of the simulation are 0.22 ± 4.2 Sv for the AMOC and 0.02 ± 0.24 PW for MHT. The
344 RMS values due to non-synopticity are on the same order as the RMS errors produced by

345 the quarterly sampling. However, since this calculation is performed over model daily values
346 instead of 7-day averages, these RMS values are actually an overestimation in comparison
347 to the other experiments.

348 2) HORIZONTAL SAMPLING

349 The AX18 XBT transect crosses three regions of different dynamic regimes (Figure 1):
350 i) the western (Confluence region), interior (gyre), and eastern (Agulhas leakage). Previous
351 studies suggest that it is critical to account for the variability in all three regions in order to
352 monitor and quantify changes in the AMOC and MHT (Dong et al. 2009). The current XBT
353 spatial sampling strategy accounts for the different regional characteristics: at a lower density
354 (~ 50 km) in the interior region, and at higher density (~ 25 km) closer to the boundaries,
355 i.e., east of the Walvis Ridge ($\sim 1^\circ\text{W}$) and west of 40°W , outside the continental slope
356 region in South America. This sampling strategy is a heuristic approach to add more spatial
357 resolution to the high energy boundary regions (Figure 1). Here we quantify the sensitivity
358 of the meridional transport changes to the horizontal sampling in these three regions. To
359 accomplish this, we generate an ensemble with 30 members by degrading the longitudinal
360 resolution in each of the three regions at a time, from the original 0.08 degree (~ 7.3 km)
361 model grid up to 5 degrees (~ 460 km) at variable steps, giving more emphasis to the high
362 resolution sampling. We use the RMS error, bias, and correlation as metrics to compare the
363 reconstructions to the original AMOC and MHT strength.

364 Our results show that the AMOC strength and MHT are less sensitive to changes in the
365 spatial resolution in the interior than at the boundary regions (Figure 8). For the AMOC,
366 degrading the resolution in the interior to a 5° degree longitude sampling produces a small
367 negative bias and RMS error of -0.6 ± 1.5 Sv, and a correlation of ~ 0.9 . In the boundary
368 regions, the AMOC and MHT are more sensitive to changes in spatial sampling. The bias
369 and RMS error for a 25 km ($\sim 0.3^\circ$) spacing is of 2.8 ± 3.2 Sv in the western and 0.23 ± 1.2
370 Sv in the eastern boundary. The correlation is about 0.9 at 25 km spacing in the boundaries,

371 and decreases to 0.6 when longitudinal sampling is larger than ~ 90 km (1°). The larger
372 decrease of correlation in the boundaries is partly due to subsampling of strong currents and
373 high mesoscale activity, and also because the shelf transport may not be observed at lower
374 sampling rates. The potentially unresolved volume transports in the continental shelves
375 (above 200 m deep) are -0.61 ± 0.77 Sv in the west and 0.15 ± 0.44 Sv in the east of
376 the basin. Both transports on the shelf contribute only a negligible temperature transport
377 ($\sim 10^{-8}$ PW), which agrees with the estimates of Baringer and Garzoli (2007). Therefore,
378 a high AX18 horizontal sampling is indeed needed in the eastern and western boundaries,
379 especially in the western side of the basin where biases are current larger in comparison to
380 the other regions.

381 Interestingly, biases in the AMOC strength and MHT have opposite signs and similar
382 magnitudes when comparing the western and eastern boundaries for any given zonal sampling
383 resolution (Figure 8c, f). Therefore, biases in the eastern and western regions may cancel
384 each other to some extent.

385 *d. AMOC and MHT uncertainties due to computational methodology*

386 In the previous section we analyzed the sensitivity of the AMOC and MHT to strategies
387 for different temporal and spatial sampling of the AX18 XBT transect. In this section, we
388 investigate how methodological assumptions affect the AMOC and MHT estimated at 34°S .
389 First, we will explore the impact of salinity and deep temperature inferences. Additionally,
390 we optimize the choice of the reference level, and propose a method to estimate the barotropic
391 velocities across the transect.

392 1) SALINITY AND DEEP TEMPERATURE INFERENCES

393 To study the impact of salinity and deep temperature inferences on the AMOC and MHT,
394 we perform step changes in the model observational strategy. We compute PSIy and MHT

395 using: i) the constructed annual T-S lookup table (Section 5a) to estimate salinity profiles
396 in the upper 800 m, ii) padding the model T-S monthly climatology in the deep ocean (>
397 800 m deep), and iii) using both the lookup table in the upper ocean and padding in the
398 deeper ocean.

399 We compare the changes in the geostrophic components of AMOC strength and MHT
400 using these approximations against those calculated using the full model output. The main
401 variability of the AMOC and MHT follow closely the ones from the approximated fields. In
402 a closer analysis of the residuals with respect to the estimates from the full model outputs
403 (Figure 9), the AMOC residuals show that the T-S lookup approximation drives most of the
404 residual changes (-0.33 ± 2.6 Sv). Residuals from the T-S lookup approximation are subject
405 to strong seasonality as observed during austral winter, when biases can reach almost -2 Sv.
406 This seasonal bias is due to the fact that the T-S relationships are taken from an annual
407 mean. Deep ocean padding biases show only a small seasonality, and AMOC mean biases
408 are small, with magnitude of 0.06 ± 2.3 Sv. For the MHT, performing either padding or TS
409 lookup approximations produce residual changes of -0.03 ± 0.14 PW and 0.02 ± 0.16 PW,
410 respectively. The RMS error calculated here is close to the value of ± 0.15 PW estimated
411 using the cumulative transport of one A10 section in Baringer and Garzoli (2007). The
412 results of our analysis using a six-year timeseries show that although the errors produced by
413 salinity and deep temperature approximations are similar in value, the seasonal amplitude
414 of the MHT and AMOC residuals using the TS lookup table is the largest (right panels
415 in Figures 9a and 9b). Although these are conservative estimates, given that the model
416 climatology represents well the variability below the surface, the errors caused by deep T-S
417 padding are small in comparison to the other sources. Thus deployment of a whole water
418 column CTD is not essential for a strong reduction of errors in the AX18 XBT transect.

420 The barotropic mode accounts for most of the bias of the overturning circulation con-
421 tribution (Baehr et al. 2004). As indicated from the model output (Figure 10), variations
422 in bottom topography are the main driver of strong bottom velocities, which increases the
423 barotropic contribution and its potential biases as well. Zonal sections, where boundaries
424 are steeper and more similar to a vertical wall, can reduce the effect of the barotropic con-
425 tribution (Rayner et al. 2011). At 34°S, where there are strong bottom velocities, strong
426 biases in the barotropic component could be introduced by assuming an inaccurate refer-
427 ence velocity (Equation 2). We estimate the sensitivity of the barotropic AMOC (PSI_{bar}) to
428 the reference level by performing four experiments: a) with zero reference velocity, b) with
429 climatological reference velocity at the western boundary, c) with climatological reference
430 velocity at the eastern boundary, and d) with climatological velocity at both western and
431 eastern boundaries. Similar to observational studies, we use in all experiments the refer-
432 ence depth at the $\sigma_2 = 37.09$. The evolution and the mean barotropic streamfunction are
433 shown in Figure 11 for each experiment. The minimum of barotropic streamfunction, which
434 characterizes its strength, is located between 2 and 3 km deep. Using model velocities, the
435 mean PSI_{bar} strength is estimated as -16.3 Sv. When zero reference velocity is assumed, a
436 much weaker PSI_{bar} strength value is estimated ($\text{PSI}_{bar} = -9.0$ Sv; Figure 11a), or a mean
437 bias of 7.2 ± 8.45 Sv. Because the barotropic streamfunction is the main balance of the
438 vertical shear component in the model (Figure 3), a weaker PSI_{bar} acts to increase the MHT
439 by 0.16 ± 0.22 . Adding a climatological reference velocity in the boundaries reduces the
440 uncertainties in the barotropic mode. The derived PSI_{bar} strength estimates using climato-
441 logical reference velocities in the boundaries produce positive biases of 5.5 ± 7.1 Sv ($0.06 \pm$
442 0.16 PW) in the western boundary and 3.5 ± 5.6 Sv (0.08 ± 0.21 PW) in the eastern side
443 of the basin (Figures 11b and 11c, respectively). Therefore, the eastern boundary velocity
444 information reduces uncertainties more than in the western boundary. When both eastern
445 and western reference velocities are added (Figure 11d), the mean $\text{PSI}_{bar} = -14.4$ Sv, and

446 the PSI_{bar} strength is correctly measured at value of 1.9 ± 4.7 Sv (0.02 ± 0.13 PW). Fur-
447 ther adding reference velocity information in the interior does not improve these uncertainty
448 values. Therefore, we show here that the misrepresentation of the reference velocities in the
449 geostrophic calculation yields the highest contribution to the uncertainties in the AMOC
450 and MHT calculations. Knowledge of the reference level velocities at both the western and
451 eastern boundaries is necessary for considerably reducing the mean bias in the barotropic
452 mode. This can be achieved by using climatological values in the boundaries, and this in-
453 formation may be acquired from available Argo float climatologies (e.g., Goes et al. 2013a),
454 for example. However, climatological reference velocities still produce relatively large biases
455 (1.9 ± 5.2 Sv and 0.02 ± 0.13 PW) due to the high variability of the barotropic mode in the
456 region. To tackle the high frequency variability of the barotropic mode, additional available
457 observations can be used. This question is addressed in the next section.

458 3) ALTERNATIVE BAROTROPIC VELOCITY ESTIMATION USING ALTIMETRY AND HY- 459 DROGRAPHY

460 In order to optimize the information necessary to monitor the AMOC at 34°S , several
461 additional observations could be used to complement the AX18 XBT transect measurements.
462 Some complimentary observations are already in place, such as the satellite wind stress
463 measurements used to estimate the Ekman transport.

464 A topic of current research in the AMOC decomposition is the estimation of the barotropic
465 mode. Using a reference level near the bottom of the ocean cannot capture interannual or
466 longer variability due to the presence of deep flows, since in this work climatology is as-
467 sumed below 800 m. Bottom pressure (P_{bot}) recorders are a useful platform to compute the
468 time varying reference level for the meridional geostrophic velocity, and, therefore, estimate
469 the non-steric component of the sea level height (SLH). Such a platform requires further
470 investment in an array across the basin, and efforts are underway (Perez et al. 2011; Meinen
471 et al. 2012). Some recent studies use a blend of altimetry and Argo parking velocity as

472 the reference level or level of known motion to infer absolute geostrophic velocities (Willis
473 and Fu 2008; Mielke et al. 2013; Goes et al. 2013a). However, because a large number of
474 Argo floats is necessary to produce a reliable estimate, seasonal averages are generally used
475 in an Argo-based reference level. We showed in the previous section that a climatological
476 assumption of the reference velocity in the eastern and western boundaries can reduce the
477 AMOC mean bias considerably. Here we test another method for measuring the barotropic
478 flow by using SLH derived from satellite altimetry in conjunction with hydrographic data.
479 Altimetry captures both steric and non-steric components, whose contributions are variable
480 among different regions of the ocean (Guinehut et al. 2006). The non-steric contribution
481 generally increases toward higher latitudes due to weaker stratification and stronger Coriolis
482 force. In some regions the non-steric contributions, such as the barotropic component, can
483 account for more than 50% of the total sea level variability (Shriver and Hurlburt 2000).

484 Using a hydrostatic relation, the non-steric sea level can be accurately related to bottom
485 and atmospheric (P_{atm}) pressure (Park and Watts 2005) as $SLH = (P_{bot} - \rho_0 g H - P_{atm}) / \rho_0 g$.
486 In order to estimate the non-steric component of the sea level, we filter the steric contribution
487 by calculating the residual between SLH and the dynamic height (DH) referenced at a certain
488 level ($SLH - DH$). The barotropic velocities are calculated using geostrophy on this residual
489 field, and the maximum barotropic streamfunction calculated from these velocities is then
490 compared to the model barotropic streamfunction.

491 We consider DH referenced at a certain depth, and estimate the optimal reference depth
492 by varying the reference of DH from 300 m down to 3500 m deep (Figure 12). According to
493 our results, the structure of the variability of the barotropic velocities can be well captured
494 by the non-steric sea level. The strength of the barotropic AMOC show correlations above
495 0.6 irrespective of the reference level used in the DH estimation. High correlations (> 0.9)
496 are found for a DH reference level between 500 m and 1000 m. A minimum RMS region
497 (< 5 Sv) overlaps with the maximum correlation region, and it is found for a reference level
498 between 700-1100 m (Figure 12a). The minimum RMS error of ~ 3 Sv is achieved when

499 DH is referenced at 1000 m. Finally, we quantify how much information is gained by using
500 altimetry data instead of using the $\sigma_2 = 37.09$ as a level of no motion for barotropic velocity.
501 The barotropic streamfunction strength using the $\sigma_2 = 37.09$ reference level shows RMS
502 error and correlation of 9 Sv and 0.78, respectively. Using altimetry and DH referenced at
503 800 m, the maximum depth of an XBT profile, promotes a gain of 4 Sv in RMS and 0.15 in
504 correlation towards this density reference level. Although we did not include measurement
505 errors in these estimates, this result is a proof of concept that altimetry and XBT data are
506 complementary platforms for the inference of the long term variability of the AMOC.

507 **6. Conclusions**

508 In this study we use a high resolution model assimilation product to assess the obser-
509 vational and computational uncertainties associated with estimating meridional transports
510 using the data from the AX18 XBT transect along 34°S. We analyzed the AMOC and MHT
511 in terms of their vertical shear, barotropic, and Ekman components. These terms are here
512 used to reconstruct the AMOC and MHT. We show that this method is well suited for this
513 type of work. In comparison to the AMOC calculated from the model velocities, the recon-
514 structed AMOC streamfunction is able to represent the main model features, although the
515 reconstruction cannot capture the high frequency reversals of the model AMOC and MHT
516 during austral winter/spring. A key finding obtained here is that XBTs produce acceptable
517 estimates of the AMOC and MHT variability, where the uncertainties obtained by the mul-
518 tiple sources of error are smaller than the signal of the time series variability. Therefore, the
519 AX18 transect is a valuable and longstanding piece of a multiple platform monitoring system
520 for the region, and efforts should be made to maintain and improve it. The results obtained
521 here are summarized in Table 1, and the results of Baringer and Garzoli (2007) for MHT is
522 added for comparison. As follows, we make recommendations for optimization of sampling
523 and computational methodologies to improve estimates of the AMOC and meridional MHT:

- 524 • The effect of T-S padding from monthly climatology below 800 m on the AMOC (0.06
525 ± 2.6 Sv) and MHT (-0.03 ± 0.14) estimates is small in comparison to the other error
526 sources. The effect of using salinity from the T-S lookup table in the upper 800 m
527 is also small in comparison to the other components, and is about the same order as
528 the deep ocean padding. However, due to seasonal biases, monthly biases can reach
529 2 Sv. Salinity from other measurements, such as Argo or monthly climatology T-S
530 relationships, would avoid these seasonal biases.

- 531 • Current quarterly sampling causes an average RMS error of ± 2.3 Sv and ± 0.24 PW
532 in the climatological AMOC and MHT estimates, respectively. The optimal strategy
533 to reduce this sampling error would be to carry out 12 transects per year, i.e. one per
534 month, which is subject to operational constraints. More realistically, it is desirable to
535 conduct continuous realizations at current quarterly sampling for at least 15 years.

- 536 • Spatial subsampling in the interior produces small errors in the AMOC and MHT
537 estimates compared to the errors produced at the boundaries. The current AX18
538 zonal sampling uses 25 km on the boundaries and 50 km in the interior of the basin.
539 This current spatial sampling seems to be adequate to capture most of the variability of
540 the meridional transports, although the western boundary resolution still shows large
541 AMOC and MHT biases at the present sampling (2.8 ± 3.2 Sv and 0.13 ± 0.14 PW).
542 An increase in the western boundary sampling to 20 km would improve current AMOC
543 results, and it would capture better the variability of the shelf transport.

- 544 • As described in previous studies (e.g., Kanzow et al. 2007, for 26.5°N), the barotropic
545 mode is likely to be the most significant source of errors in the AMOC and MHT
546 calculations due to the extensive continental shelf along 34°S . Errors are on the order
547 of 7.2 ± 8.45 Sv for the AMOC and 0.16 ± 0.22 PW for MHT if a level of no motion
548 is used in $\sigma_2 = 37.09 \text{ kgm}^{-3}$. Using at least climatological values as the reference
549 velocities in both boundaries is necessary to reduce the AMOC and MHT biases to \sim

550 1.9 ± 5.2 Sv and 0.02 ± 0.13 PW, respectively.

- 551 • The use of satellite altimetry observations in conjunction with hydrographic data is
552 a good alternative for barotropic term estimation. We show that barotropic volume
553 transport estimates using the non-steric component of altimetry can improve the RMS
554 error by ~ 3 Sv in comparison to the commonly used level of no motion at $\sigma_2 = 37.09$
555 kgm^{-3} .

556 Finally, this study assesses only one the part of the several platforms that are in place to
557 monitor the variability of the AMOC and MHT in the South Atlantic, XBT and altimetry
558 data. The utility of the other operational platforms, such as moorings and Argo data, has
559 been demonstrated in various other studies (Dong et al. 2011a; Perez et al. 2011). An
560 analysis that includes a blend of several platforms is still necessary to evaluate the optimal
561 observational system for the region.

562 *Acknowledgments.*

563 The authors want to thank Joe Metzger for providing the GLBa0.08/74.2 simulation
564 output, and the ship companies Evergreen Lines, CMA CGM Lines, Hamburg Sud and Monte
565 Azul for carrying out the AX18 cruises as part of the Ships of Opportunity project. This
566 research was accomplished under the auspices of the Cooperative Institute for Marine and
567 Atmospheric Studies (CIMAS), a cooperative institute of the University of Miami and the
568 National Oceanic and Atmospheric Administration, cooperative agreement #NA17RJ1226,
569 and was partly funded by the NOAA Climate Program Office.

REFERENCES

- 572 Baehr, J., J. Hirschi, J.-O. Beismann, and J. Marotzke, 2004: Monitoring the meridional
573 overturning circulation in the North Atlantic: A model-based array design study. *J. Mar.*
574 *Res.*, **62** ((3)), 283–312, doi:10.1357/0022240041446191.
- 575 Baehr, J., D. McInerney, K. Keller, and J. Marotzke, 2008: Optimization of an observ-
576 ing system design for the North Atlantic meridional overturning circulation. *Journal of*
577 *Atmospheric and Oceanic Technology*, **25** (4), 625–634, doi:10.1175/2007JTECHO535.1.
- 578 Baringer, M. and S. Garzoli, 2007: Meridional heat transport determined with expendable
579 bathythermographs, Part I: Error estimates from model and hydrographic data. *Deep-Sea*
580 *Res. I*, **54** (8), 1390–1401, doi:10.1016/j.dsr.2007.03.011.
- 581 Beal, L. M., W. P. M. D. Ruijter, A. Biastoch, R. Zahn, and S. 136, 2011: On the role
582 of the Agulhas system in ocean circulation and climate. *Nature*, **472** (7344), 429–436,
583 doi:10.1038/nature09983.
- 584 Biastoch, A., C. W. Boning, F. U. Schwarzkopf, and J. R. E. Lutjeharms, 2009: Increase
585 in Agulhas leakage due to poleward shift in the southern hemisphere westerlies. *Nature*,
586 **462**, 495–498, doi:10.1038/nature08519.
- 587 Bryden, H. L., H. R. Longworth, and S. A. Cunningham, 2005: Slowing of the Atlantic merid-
588 ional overturning circulation at 25°N. *Nature*, **438**, 655–657, doi:10.1038/nature04385.
- 589 Chassignet, E., et al., 2009: U.S. GODAE: Global ocean prediction with the hybrid coordi-
590 nate ocean model (HYCOM). *Oceanography*, **22** (2), 64–75, doi:10.5670/oceanog.2009.39.
- 591 Cummings, J. A., 2005: Operational multivariate ocean data assimilation. *Quart. J. Royal*
592 *Met. Soc., Part C*, **131** (613), 3583–3604, doi:10.1256/qj.05.105.

593 Dong, S., M. Baringer, G. Goni, and S. Garzoli, 2011a: Importance of the assimilation of
594 argo float measurements on the meridional overturning circulation in the south atlantic.
595 *Geophys. Res. Lett.*, **38**, L18 603, doi:10.1029/2011GL048982.

596 Dong, S., S. Garzoli, and M. Baringer, 2011b: The role of interocean exchanges on decadal
597 variations of the meridional heat transport in the South Atlantic. *J. Phys. Oceanogr.*, **41**,
598 1498–1511, doi:10.1175/2011JPO4549.1.

599 Dong, S., S. L. Garzoli, M. O. Baringer, C. S. Meinen, and G. J. Goni, 2009: Interannual
600 variations in the Atlantic meridional overturning circulation and its relationship with the
601 net northward heat transport in the South Atlantic. *Geophys. Res. Lett.*, **36**, L20 606,
602 doi:10.1029/2009GL039356.

603 Donners, J. and S. S. Drijfhout, 2004: The lagrangian view of South Atlantic interocean
604 exchange in a global ocean model compared with inverse model results. *J. Phys. Oceanogr.*,
605 **34**, 1019–1035, doi:10.1175/1520-0485(2004)034<1019:TLVOSA>2.0.CO;2.

606 Ducet, N., P.-Y. L. Traon, and G. Reverdin, 2000: Global high-resolution mapping of ocean
607 circulation from Topex/Poseidon and ERS-1 and -2. *J. Geophys. Res.*, **105 (C8)**, 19 477–
608 19 498, doi:10.1029/2000JC900063.

609 Fox, D., W. J. Teague, C. N. Barron, M. R. Carnes, and C. M. Lee, 2002: The modular
610 ocean data assimilation system (MODAS). *J. Atmos. Ocean. Technol.*, **19**, 240–252, doi:
611 10.1175/1520-0426(2002)019<0240:TMODAS>2.0.CO;2.

612 Ganachaud, A. and C. Wunsch, 2003: Large scale ocean heat and freshwater transports
613 during the World Ocean Circulation Experiment. *J. Climate*, **16**, 696–705, doi:10.1175/
614 1520-0442(2003)016<0696:LSOHAF>2.0.CO;2.

615 Garzoli, S., 1993: Geostrophic velocities and transport variability in the Brazil/Malvinas
616 confluence. *Deep-Sea Res.*, **40**, 1379–1403, doi:10.1016/0967-0637(93)90118-M.

617 Garzoli, S. and M. Baringer, 2007: Meridional heat transport determined with expendable
618 bathythermographs. Part II: South Atlantic transport. *Deep-Sea Res. I*, **54**, 1402–1420,
619 doi:10.1016/j.dsr.2007.04.013.

620 Garzoli, S., M. Baringer, S. Dong, R. Perez, and Q. Yao, 2013: South Atlantic meridional
621 fluxes. *Deep-Sea Res. I*, **71**, 21–32, doi:10.1016/j.dsr.2012.09.003.

622 Garzoli, S. L. and R. Matano, 2011: The South Atlantic and the Atlantic meridional over-
623 turning circulation. *Deep-Sea Res. Part II*, **58 (17–18)**, 1837–1847, doi:10.1016/j.dsr2.
624 2010.10.063.

625 Goes, M., G. Goni, V. Hormann, and R. Perez, 2013a: Variability of the Atlantic off-
626 equatorial eastward currents during 1993-2010 using a synthetic method. *J. Geophys.*
627 *Res.-Oceans*, **118 (6)**, 3026 – 3045, doi:10.1002/jgrc.20186.

628 Goes, M., G. Goni, and K. Keller, 2013b: Reducing biases in XBT measurements by includ-
629 ing discrete information from pressure switches. *J. Atmos. Oceanic Technol.*, **30**, 810–824,
630 doi:10.1175/JTECH-D-12-00126.1.

631 Goni, G., F. Bringas, and P. D. Nezio, 2011: Observed low frequency variability of the Brazil
632 Current front. *J. Geophys. Res.*, **116**, C10 037, doi:10.1029/2011JC007198.

633 Goni, G., S. Garzoli, A. Roubicek, D. Olson, and O. Brown, 1997: Agulhas ring dynamics
634 from TOPEX/POSEIDON satellite altimeter data. *Journal of Marine Research*, **55 (5)**,
635 861–883, doi:10.1357/0022240973224175.

636 Goni, G. and I. Wainer, 2001: Investigation of the Brazil Current front variability from
637 altimeter data. *J. Geophys. Res.*, **106**, 31 117–31 128, doi:10.1029/2000JC000396.

638 Gordon, A., 1986: Interocean exchange of thermocline water. *J. Geophys. Res.*, **91**, 5037–
639 5046, doi:10.1029/JC091iC04p05037.

- 640 Griffies, S. M., M. J. Harrison, R. C. Pacanowski, and A. Rosati, 2004: A technical guide
641 to MOM4. *GFDL Ocean Group Technical Report No. 5*, Princeton, NJ.: NOAA/GFDL,
642 342 pp.
- 643 Guinehut, S., P.-Y. L. Traon, and G. Larnicol, 2006: What can we learn from global
644 altimetry/hydrography comparisons? *Geophys. Res. Lett.*, **33**, L10 604, doi:10.1029/
645 2005GL025551.
- 646 Hall, M. M. and H. L. Bryden, 1982: Direct estimates and mechanisms of ocean heat trans-
647 port. *Deep-Sea Res.*, **29 (3)**, 339–359, doi:10.1016/0198-0149(82)90099-1.
- 648 Hawkings, E., R. S. Smith, L. C. Allison, J. M. Gregory, T. J. Woollings, H. Pohlmann,
649 and B. de Cuevas, 2011: Bistability of the Atlantic overturning circulation in a global
650 climate model and links to ocean freshwater transport. *Geophys Res Lett.*, **38**, L10 605,
651 doi:10.1029/2011GL047208.
- 652 Hirschi, J., J. Baehr, J. Marotzke, J. Stark, S. Cunningham, and J.-O. Beismann, 2003:
653 A monitoring design for the Atlantic meridional overturning circulation. *Geophysical Re-*
654 *search Letters*, **30**, 1413, doi:10.1029/2002GL016776.
- 655 Jayne, S. R. and J. Marotzke, 2001: The dynamics of ocean heat transport variability.
656 *Reviews of Geophysics*, **39**, 385–411, doi:10.1029/2000RG000084.
- 657 Kanzow, T., et al., 2007: Observed flow compensation associated with the MOC at 26.5
658 degrees N in the Atlantic. *Science*, **317 (5840)**, 938–941, doi:10.1126/science.1141293.
- 659 Lee, T. and J. Marotzke, 1998: Seasonal cycles of meridional overturning and heat trans-
660 port of the Indian Ocean. *J. Phys. Oceanogr.*, **28**, 923–943, doi:10.1175/1520-0485(1998)
661 028<0923:SCOMOA>2.0.CO;2.
- 662 Lentini, C., G. Goni, and D. Olson, 2006: Investigation of Brazil Current rings in the
663 confluence region. *J. Geophys. Res.*, **111 (C06013)**, doi:10.1029/2005JC002988.

- 664 Locarnini, R. A., A. V. Mishonov, J. I. Antonov, T. P. Boyer, and H. E. Garcia, 2006: World
665 Ocean Atlas 2005, Volume 1: Temperature. *NOAA Atlas NESDIS 61*, U.S. Government
666 Printing Office, Washington, D.C., 182 pp.
- 667 Meinen, C. S., A. R. Piola, R. C. Perez, and S. L. Garzoli, 2012: Deep Western Boundary
668 Current transport variability in the South Atlantic: preliminary results from a pilot array
669 at 34.5° S. *Ocean Sci. Discuss.*, **9**, 977–1008, doi:10.5194/osd-9-977-2012.
- 670 Mielke, C., E. Frajka-Williams, and J. Baehr, 2013: Observed and simulated variability
671 of the AMOC at 26°N and 41°N. *Geophysical Research Letters*, **40** (6), 1159–1164, doi:
672 10.1002/grl.50233.
- 673 Montgomery, R. B., 1974: Comments on Seasonal variability of the Florida current, by Niiler
674 and Richardson. *J. Mar. Res.*, **32**, 533–535.
- 675 Park, J.-H. and D. R. Watts, 2005: Response of the southwestern Japan/East Sea to the
676 atmospheric pressure. *Deep-Sea Res. II*, **52**, 1671–1683, doi:10.1016/j.dsr2.2003.08.007.
- 677 Perez, R. C., S. L. Garzoli, C. Meinen, and R. P. Matano, 2011: Geostrophic velocity
678 measurement techniques for the meridional overturning circulation and meridional heat
679 transport in the South Atlantic. *J. Atmos. and Ocean. Tech.*, **28** (11), 1504–1521, doi:
680 10.1175/JTECH-D-11-00058.1.
- 681 Pond, S. and G. Pickard, 1983: *Introductory Dynamical Oceanography*. Pergamon in-
682 ternational library of science, technology, engineering and social studies, Butterworth-
683 Heinemann, URL <http://books.google.com/books?id=5pQf8dBYxIUC>.
- 684 Rahmstorf, S., 1996: On the freshwater forcing and transport of the Atlantic thermohaline
685 circulation. *Clim. Dyn.*, **12**, 799–811, doi:10.1007/s003820050144.
- 686 Rayner, D., et al., 2011: Monitoring the Atlantic meridional overturning circulation. *Deep-*
687 *Sea Res. II*, **58** (17–18), 1744–1753, doi:10.1016/j.dsr2.2010.10.056.

- 688 Richardson, P. and S. Garzoli, 2003: Characteristics of intermediate water flow in the
689 Benguela Current as measured with RAFOS floats. *Deep-Sea Res.*, **50**, 87–118, doi:
690 10.1016/S0967-0645(02)00380-6.
- 691 Shriver, J. F. and H. E. Hurlburt, 2000: The effect of upper ocean eddies on the non-steric
692 contribution to the barotropic mode. *Geophys. Res. Lett.*, **27**, 2713–2716, doi:10.1029/
693 1999GL011105.
- 694 Sime, L. C., D. P. Stevens, K. J. Heywood, and K. I. Oliver, 2006: A decomposition of the
695 Atlantic meridional overturning. *Journal of Physical Oceanography*, **36** (**12**), 2253–2270,
696 doi:10.1175/JPO2974.1.
- 697 Stramma, L. and M. England, 1999: On the water masses and mean circulation of the South
698 Atlantic Ocean. *J. Geophys. Res.*, **104** ((**C9**)), 20 863–20 883, doi:10.1029/1999JC900139.
- 699 Thacker, W. C., 2008: Estimating salinity between 25° and 45°S in the Atlantic ocean using
700 local regression. *J. Atmos. Ocean. Tech.*, **25**, 114–130, doi:10.1175/2007JTECHO530.1.
- 701 Treguier, A. M., M. England, S. R. Rintoul, G. Madec, J. L. Sommer, and J.-M. Molines,
702 2007: Southern Ocean overturning across streamlines in an eddy simulation of the
703 Antarctic circumpolar current. *Ocean Sci.*, **3**, 491–507, doi:10.5194/os-3-491-2007.
- 704 Wainer, I., P. Gent, and G. Goni, 2000: Annual cycle of the Brazil-Malvinas confluence region
705 in the National Center for Atmospheric Research climate system model. *J. Geophys. Res.*,
706 **05** ((**C11**)), 26,167–26,177, doi:10.1029/1999JC000134.
- 707 Weijer, W., W. P. M. D. Ruijter, H. A. Dijkstra, and P. J. van Leeuwen, 1999: Impact
708 of interbasin exchange on the Atlantic overturning circulation. *J. Phys. Oceanogr.*, **29**,
709 2266–2284.
- 710 Willis, J. and L.-L. Fu, 2008: Combining altimeter and subsurface float data to estimate the

711 time-averaged circulation in the upper ocean. *J. Geophys. Res.*, **113 (C12)**, 2156–2202,
712 doi:10.1029/2007JC004690.

713 Zhang, R. and T. L. Delworth, 2005: Simulated tropical response to a substantial weakening
714 of the Atlantic thermohaline circulation. *J. Clim.*, **18**, 1853–1860, doi:10.1175/JCLI3460.1.

715 **7. Figures and tables**

716 **List of Tables**

717 1 Bias \pm RMS error of the AMOC (Sv) and MHT (PW) introduced by each
718 source of error associated with the AX18 XBT transect observational assump-
719 tions estimated in the present study. Last column shows the error estimates
720 of Baringer and Garzoli (2007), Table 3. 32

TABLE 1. Bias \pm RMS error of the AMOC (Sv) and MHT (PW) introduced by each source of error associated with the AX18 XBT transect observational assumptions estimated in the present study. Last column shows the error estimates of Baringer and Garzoli (2007), Table 3.

Source	AMOC (Sv)		Meridional Heat Transport (PW)
	Present	Present	B&G
Upper ocean salinity	-0.3 ± 2.6	0.02 ± 0.16	0.03
Deep climatology below 800 m	0.06 ± 2.3	-0.03 ± 0.14	0.15
Mass imbalance	0.9 ± 3.8	-0.02 ± 0.06	0.02
Non-synopticity	0.2 ± 4.2	0.02 ± 0.24	–
Fall rate equation error (2% of depth)	-0.06 ± 0.07	-0.01 ± 0.01	–
Quarterly sampling	± 2.3	± 0.24	–
Unresolved western shelf transport	-0.6 ± 0.8	10^{-8}	0.01
Unresolved eastern shelf transport	0.15 ± 0.4	10^{-8}	0.01
Western Horizontal resolution	2.8 ± 3.2	0.13 ± 0.14	–
Eastern Horizontal resolution	0.2 ± 1.2	0.02 ± 0.04	–
Interior Horizontal resolution	-0.4 ± 1.0	0.06 ± 0.07	–
Western Reference level	5.5 ± 7.1	0.06 ± 0.16	0.05
Eastern Reference level	3.5 ± 5.6	0.08 ± 0.21	0.05

721 List of Figures

- 722 1 Eddy kinetic energy ($\text{cm}^2 \text{s}^{-2}$) calculated from sea level anomalies for the
723 period between 2007 and 2013. (a) AVISO observations, (b) HYCOM model,
724 and (c) HYCOM minus observations. The black lines in Figure 1a are the
725 locations of the 18 selected AX18 transects between 2002 and 2012, overlaid
726 by the mean AX18 transect location in red. 36
- 727 2 (a) – (c) Sea level anomaly (SLA) root-mean-square (RMS) contours (in cm)
728 for: (a) AVISO overlaid by the mean AX18 transect (magenta line); (b) HY-
729 COM/NCODA; (c) HYCOM/NCODA minus AVISO. (d)–(i): Mean tem-
730 perature sections contours (in $^{\circ}\text{C}$) for: (d, g) observations, with AX18 data
731 for the upper 850 m (d) and WOA05 for 850 m to bottom (g); (e, h) HY-
732 COM/NCODA model; (f, i) HYCOM/NCODA minus observations. 37
- 733 3 (a) Maximum volume transport streamfunction (AMOC) using model veloc-
734 ities (black) and the reconstruction (magenta). (b) AMOC decomposition
735 into vertical shear (red), Ekman (blue), and barotropic (green) components.
736 (c) Time mean meridional transport streamfunction for the model velocities
737 (black), reconstruction (magenta), Ekman (blue), vertical shear (red) and
738 barotropic (green). 38
- 739 4 (a) Heat transport (MHT in PW) using model velocities (black) and recon-
740 struction (magenta). (b) MHT decomposition into vertical shear (red), Ekman
741 (blue), and barotropic (green) components. 39
- 742 5 Monthly means of the (a) AMOC and (b) MHT components: vertical shear
743 (red), Ekman (blue) and barotropic (green). The level of reference is assumed
744 to be on the ocean bottom using the model bottom velocities as the refer-
745 ence. The sum of the transport components (gray) is comparable to the total
746 transport from the original model velocities (black). 40

747	6	RMS error between the estimated salinity using climatological T-S relationships and the model salinity along the 34.5°S section.	41
748			
749	7	RMS error of geostrophic AMOC (a) and MHT (b) associated with different time samplings, i.e., the number of samples per year (y-axis) and the number of year (x-axis). The RMS error is calculated from the difference between the reconstructed time series using a different time sampling and the reconstructed time series using the original model sampling. The number of samples per year is randomly selected, and this process is realized 400 times to average the random realizations. The stars in (a) and (b) correspond to the current location of the AX18 sampling in the time sampling parameter space.	42
750			
751			
752			
753			
754			
755			
756			
757	8	RMS error, correlation, and bias of the AMOC (a, b, c) and MHT (d, e, f) with respect to the simulated longitudinal resolution (in degrees) of the AX18 transect. The transect horizontal resolution varies individually for three regions, western boundary (red), interior (blue) and eastern boundary (black). The x-axis is shown in logarithmic scale.	43
758			
759			
760			
761			
762	9	Anomalies relative to the total model field time series of (a) geostrophic AMOC and (b) MHT, and respective monthly averages (right panels). The total field anomalies are defined as having zero value (black), and the colored time series assume a bottom T-S climatology padding (red), salinity inference from lookup table in the top 800 m (blue), padding plus T-S lookup (green), and the total (black).	44
763			
764			
765			
766			
767			
768	10	Barotropic velocities at 34.5°S estimated from the model velocities. The top panel shows the average depth of the $\sigma_2 = 37.9$ (red line) overlaid on model bathymetry	45
769			
770			

- 771 11 Changes in the barotropic streamfunction (Sv) due to the knowledge of a
772 climatological reference velocity at $\sigma_2 = 37.09$. (a) Zero reference velocity,
773 (b) eastern boundary, (c) western boundary, and (d) western plus eastern
774 boundaries. Left panels: time evolution of the barotropic streamfunction.
775 Right panels: respective time average of the barotropic streamfunction. 46
- 776 12 a) RMS error and (b) correlation between the barotropic streamfunction
777 strength for the barotropic velocities calculated from the SLH-DH residual
778 with a variable reference level from 300 m to 3500 m depth (x-axis). Also
779 added for comparison the RMS and correlation of the streamfunction strength
780 for barotropic velocities calculated using a reference at a level of no motion
781 at $\sigma_2 = 37.09 \text{ kg m}^{-3}$. 47

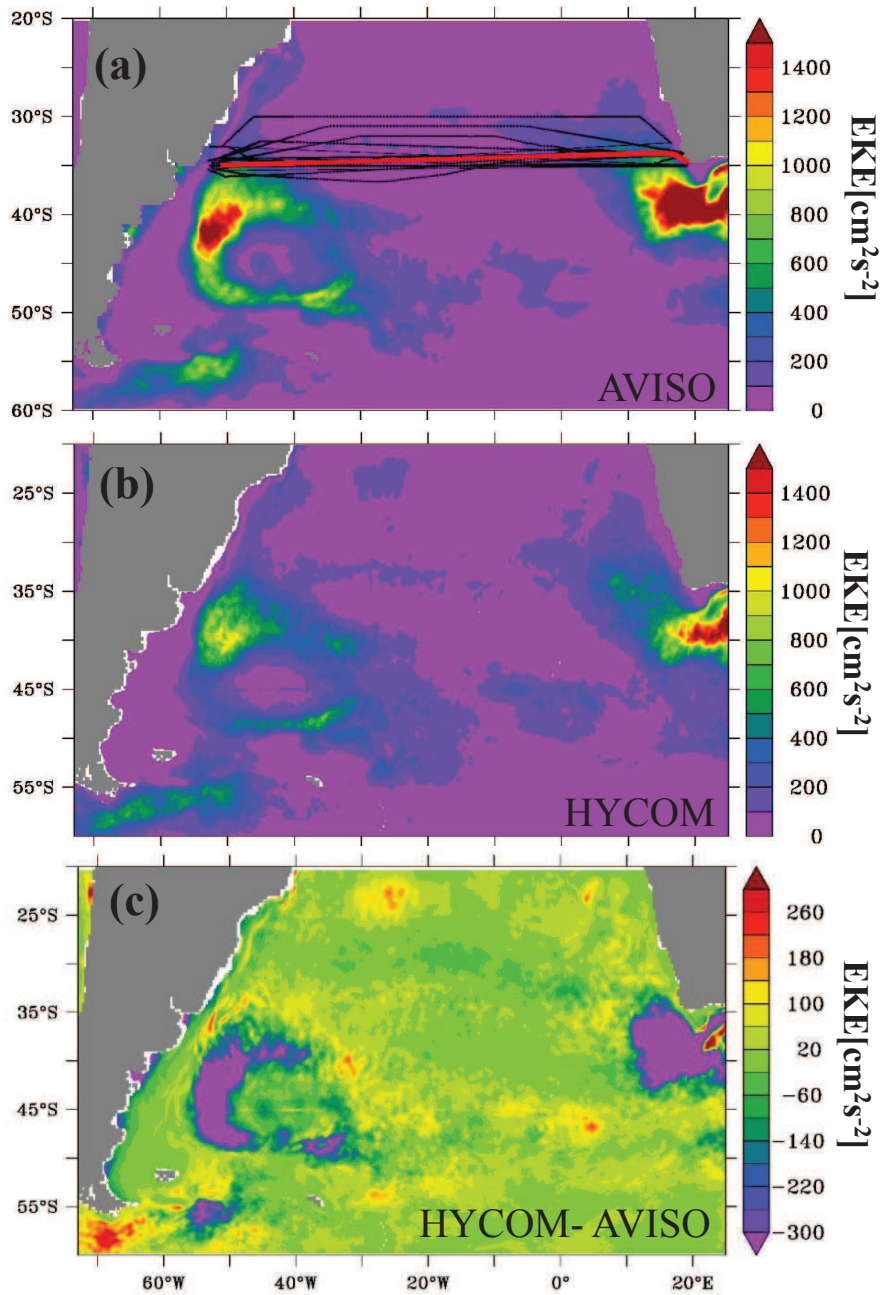


FIG. 1. Eddy kinetic energy ($\text{cm}^2 \text{s}^{-2}$) calculated from sea level anomalies for the period between 2007 and 2013. (a) AVISO observations, (b) HYCOM model, and (c) HYCOM minus observations. The black lines in Figure 1a are the locations of the 18 selected AX18 transects between 2002 and 2012, overlaid by the mean AX18 transect location in red.

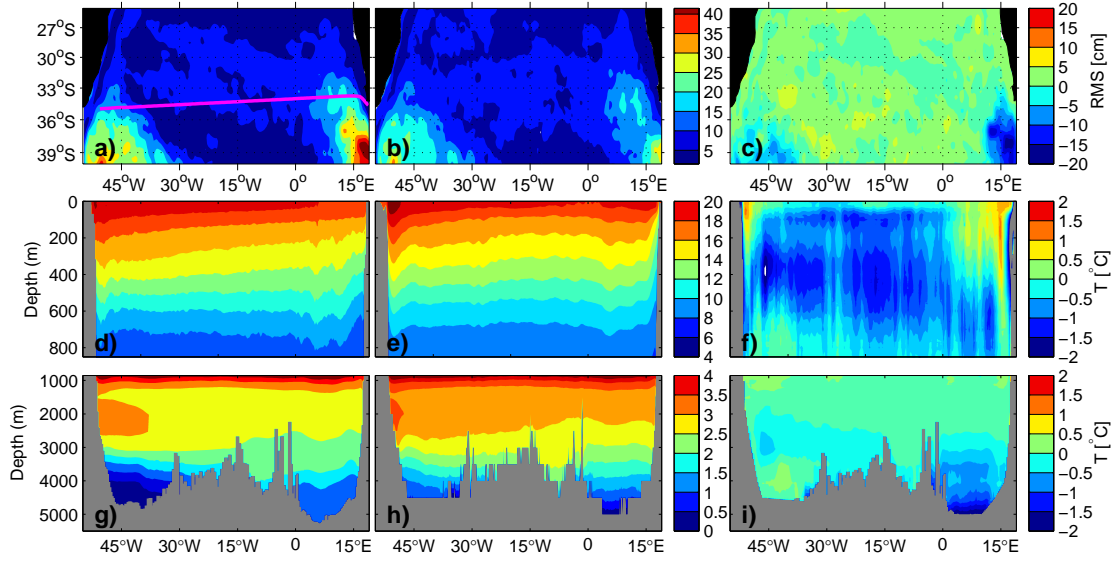


FIG. 2. (a) – (c) Sea level anomaly (SLA) root-mean-square (RMS) contours (in cm) for: (a) AVISO overlaid by the mean AX18 transect (magenta line); (b) HYCOM/NCODA; (c) HYCOM/NCODA minus AVISO. (d)–(i): Mean temperature sections contours (in °C) for: (d, g) observations, with AX18 data for the upper 850 m (d) and WOA05 for 850 m to bottom (g); (e, h) HYCOM/NCODA model; (f, i) HYCOM/NCODA minus observations.

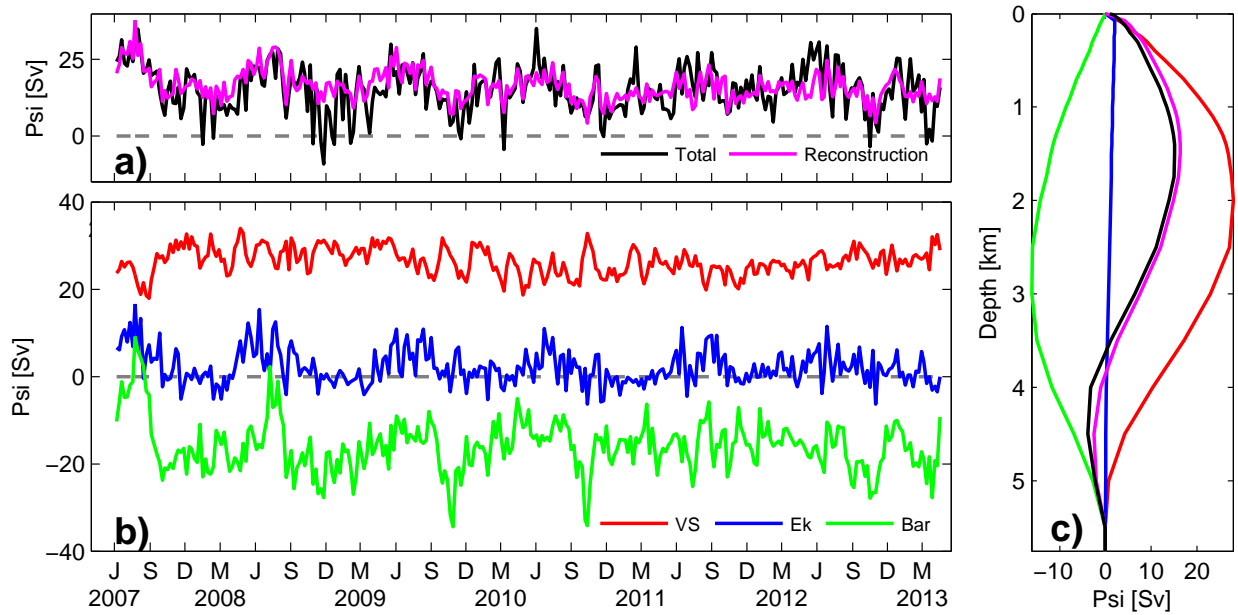


FIG. 3. (a) Maximum volume transport streamfunction (AMOC) using model velocities (black) and the reconstruction (magenta). (b) AMOC decomposition into vertical shear (red), Ekman (blue), and barotropic (green) components. (c) Time mean meridional transport streamfunction for the model velocities (black), reconstruction (magenta), Ekman (blue), vertical shear (red) and barotropic (green).

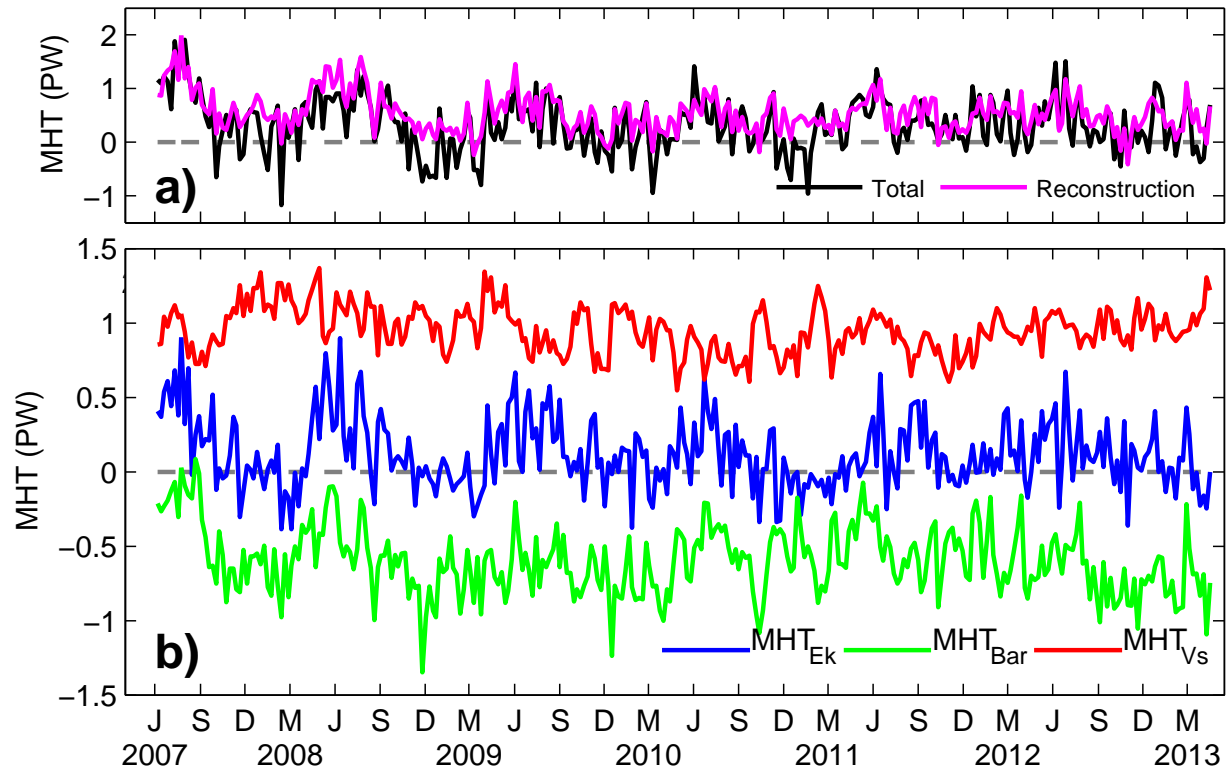


FIG. 4. (a) Heat transport (MHT in PW) using model velocities (black) and reconstruction (magenta). (b) MHT decomposition into vertical shear (red), Ekman (blue), and barotropic (green) components.

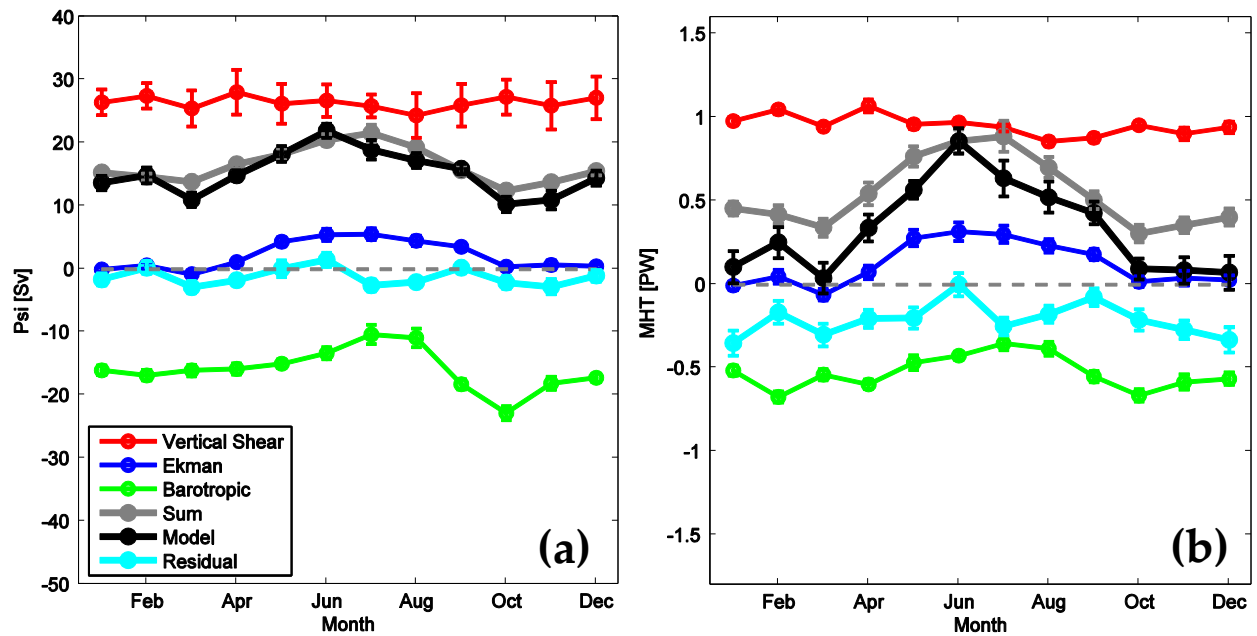


FIG. 5. Monthly means of the (a) AMOC and (b) MHT components: vertical shear (red), Ekman (blue) and barotropic (green). The level of reference is assumed to be on the ocean bottom using the model bottom velocities as the reference. The sum of the transport components (gray) is comparable to the total transport from the original model velocities (black).

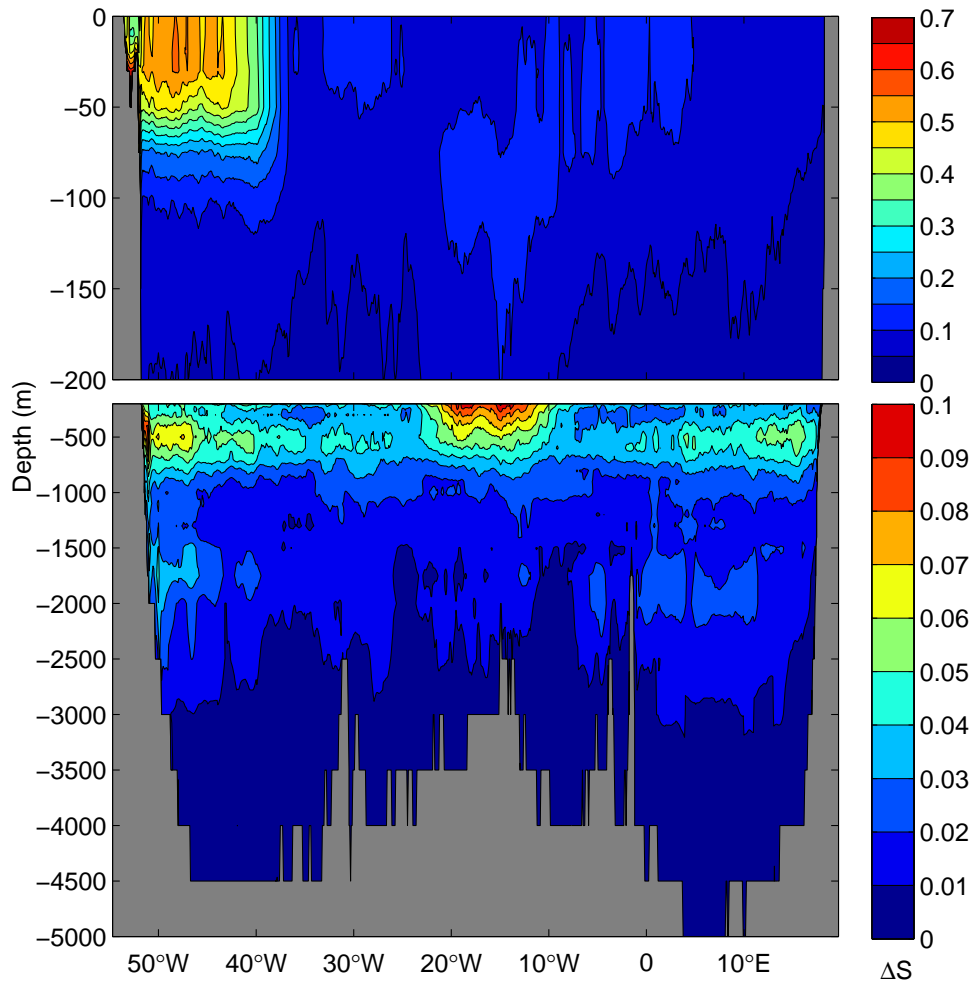


FIG. 6. RMS error between the estimated salinity using climatological T-S relationships and the model salinity along the 34.5°S section.

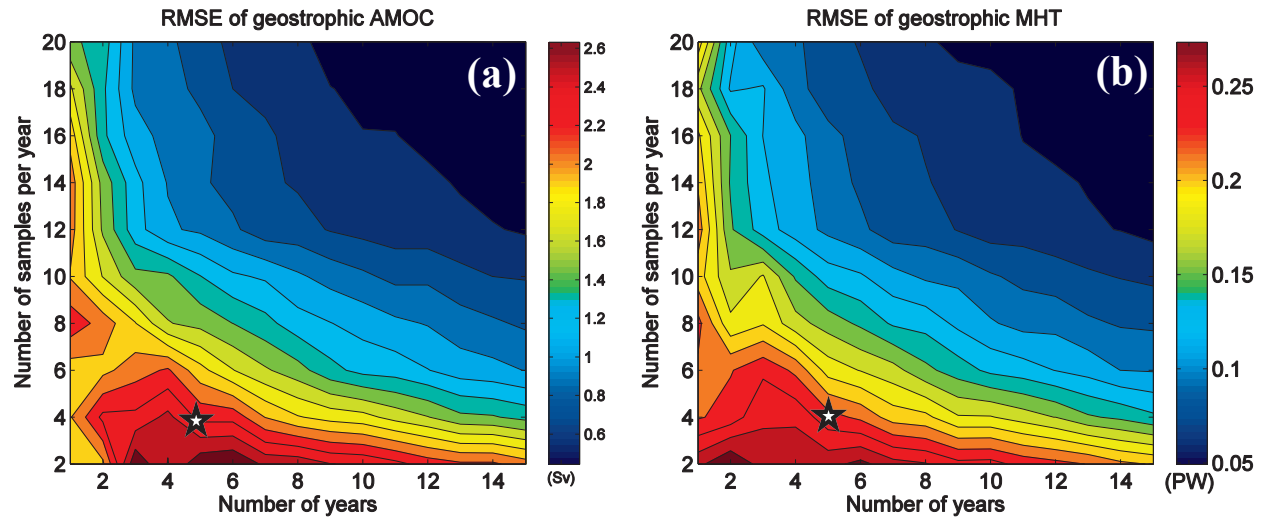


FIG. 7. RMS error of geostrophic AMOC (a) and MHT (b) associated with different time samplings, i.e., the number of samples per year (y-axis) and the number of year (x-axis). The RMS error is calculated from the difference between the reconstructed time series using a different time sampling and the reconstructed time series using the original model sampling. The number of samples per year is randomly selected, and this process is realized 400 times to average the random realizations. The stars in (a) and (b) correspond to the current location of the AX18 sampling in the time sampling parameter space.

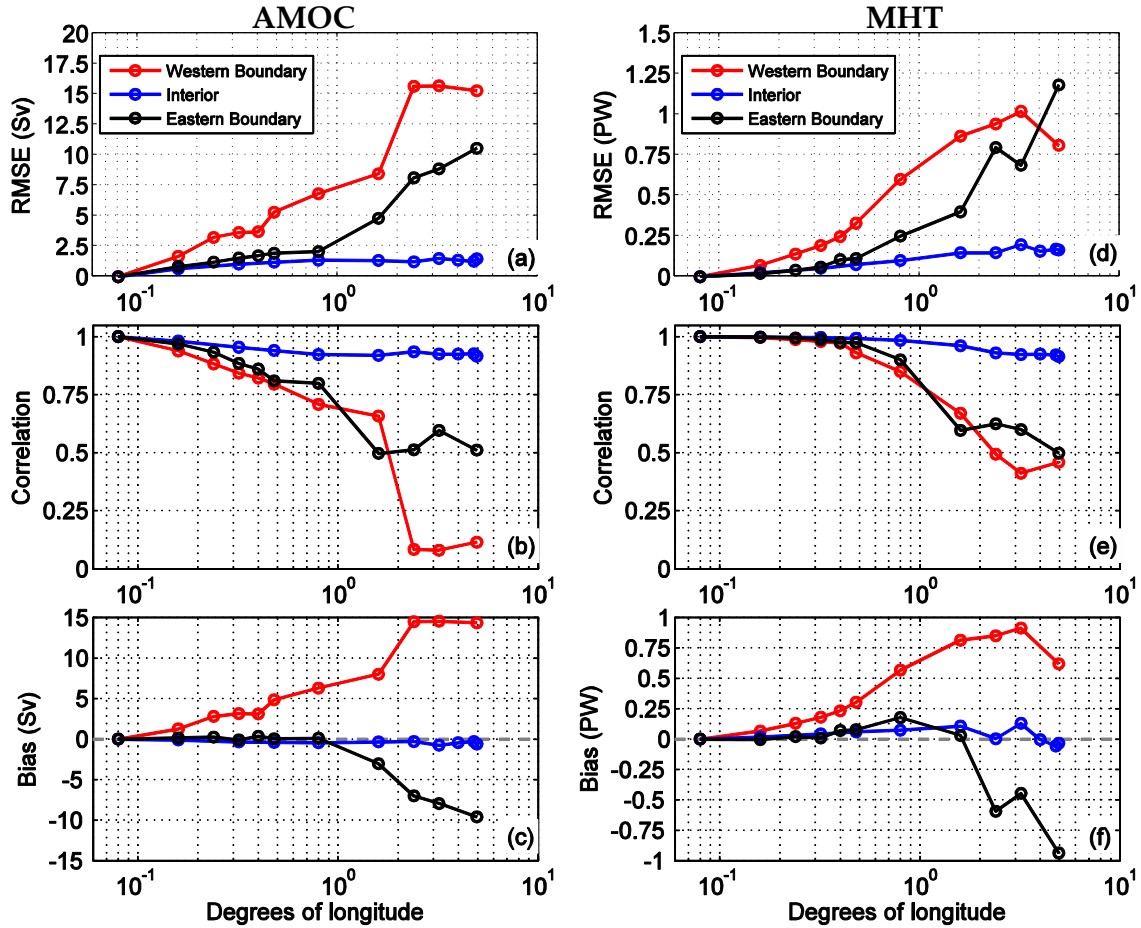


FIG. 8. RMS error, correlation, and bias of the AMOC (a, b, c) and MHT (d, e, f) with respect to the simulated longitudinal resolution (in degrees) of the AX18 transect. The transect horizontal resolution varies individually for three regions, western boundary (red), interior (blue) and eastern boundary (black). The x-axis is shown in logarithmic scale.

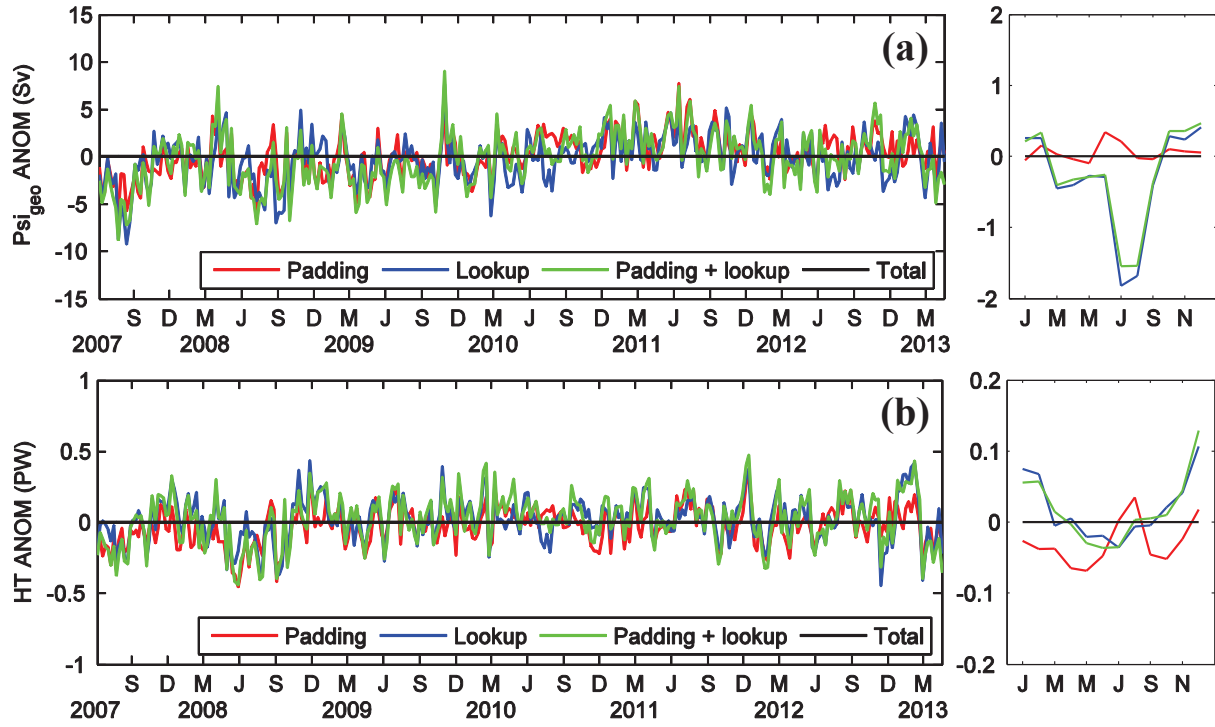


FIG. 9. Anomalies relative to the total model field time series of (a) geostrophic AMOC and (b) MHT, and respective monthly averages (right panels). The total field anomalies are defined as having zero value (black), and the colored time series assume a bottom T-S climatology padding (red), salinity inference from lookup table in the top 800 m (blue), padding plus T-S lookup (green), and the total (black).

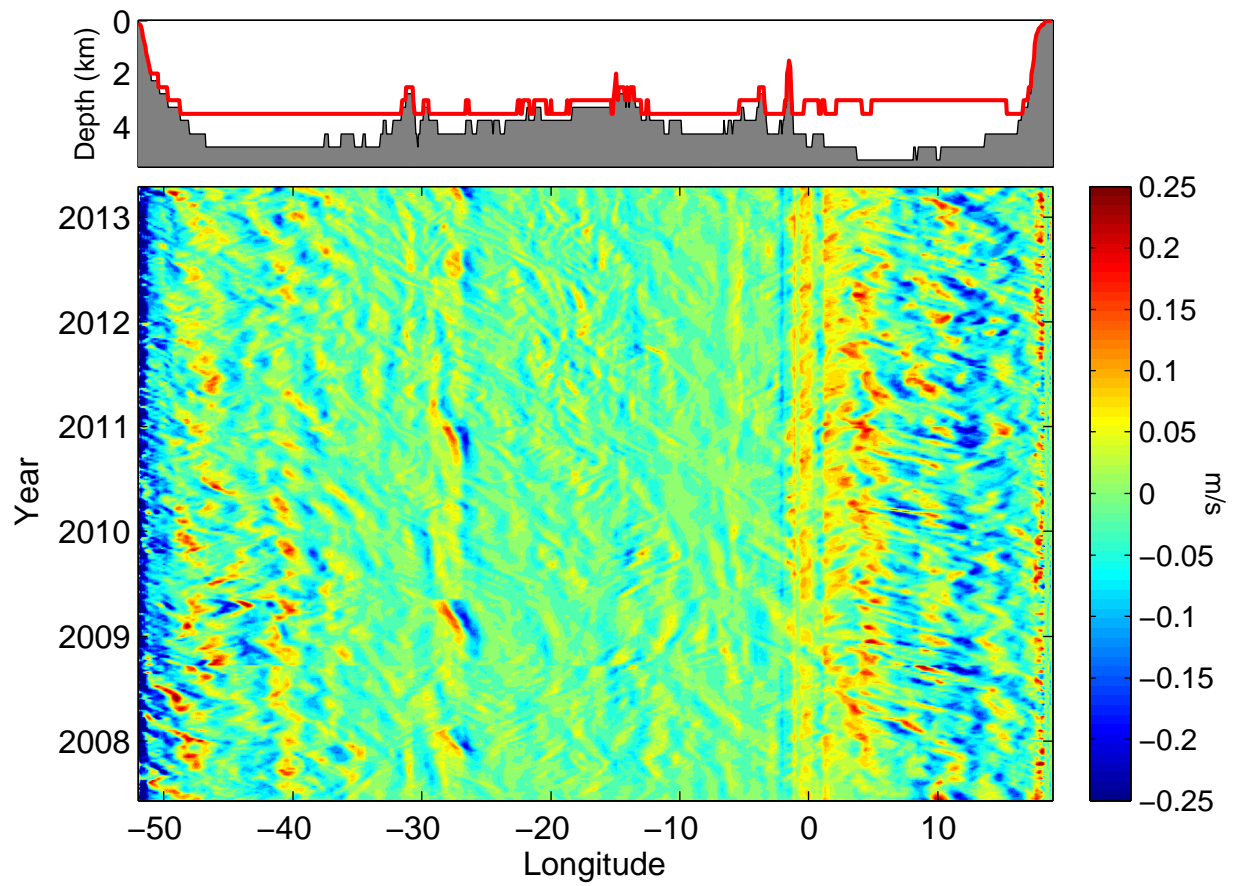


FIG. 10. Barotropic velocities at 34.5°S estimated from the model velocities. The top panel shows the average depth of the $\sigma_2 = 37.9$ (red line) overlaid on model bathymetry

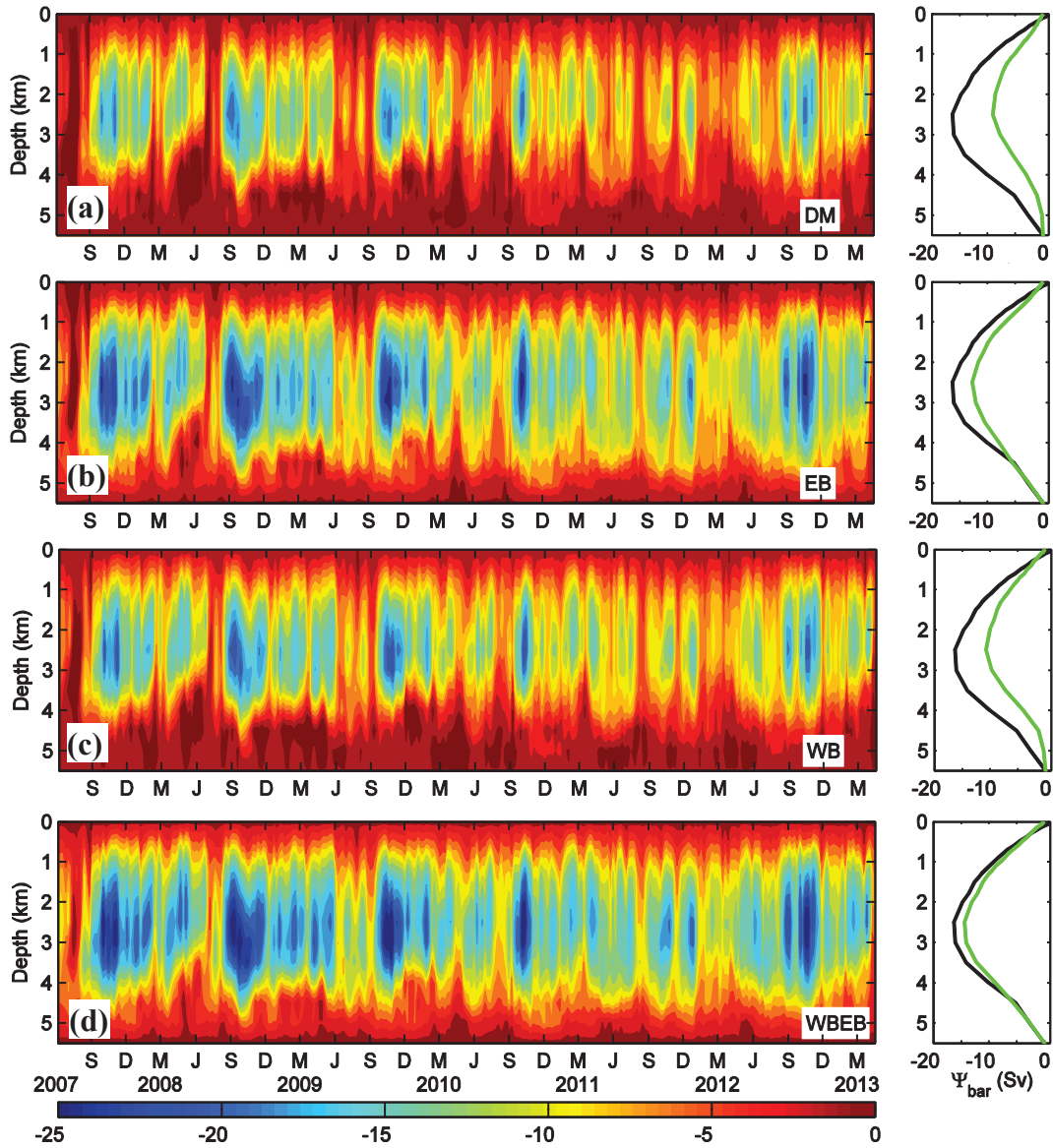


FIG. 11. Changes in the barotropic streamfunction (Sv) due to the knowledge of a climatological reference velocity at $\sigma_2 = 37.09$. (a) Zero reference velocity, (b) eastern boundary, (c) western boundary, and (d) western plus eastern boundaries. Left panels: time evolution of the barotropic streamfunction. Right panels: respective time average of the barotropic streamfunction.

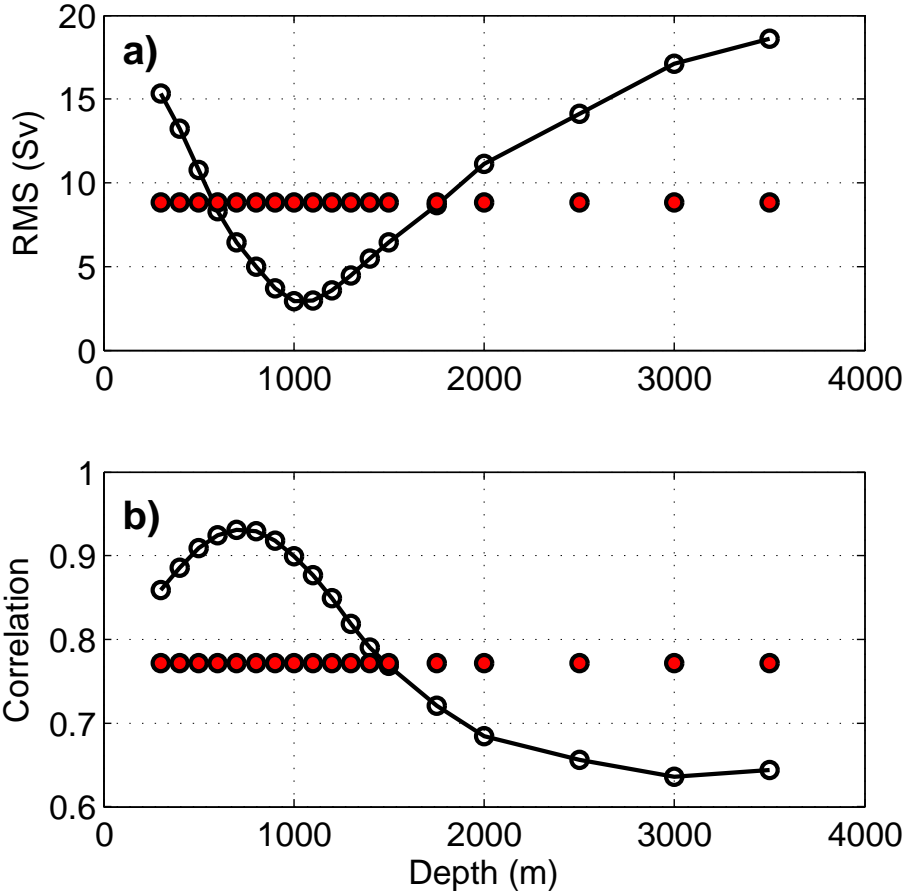


FIG. 12. a) RMS error and (b) correlation between the barotropic streamfunction strength for the barotropic velocities calculated from the SLH-DH residual with a variable reference level from 300 m to 3500 m depth (x-axis). Also added for comparison the RMS and correlation of the streamfunction strength for barotropic velocities calculated using a reference at a level of no motion at $\sigma_2 = 37.09 \text{ kg m}^{-3}$.